

Control of Turbulent Flow over a Circular Cylinder Using Tabs

Junyoung Seo, Jinhyeok Yun  and Jungil Lee * 

Department of Mechanical Engineering, Ajou University, Suwon 16499, Republic of Korea

* Correspondence: jungillee@ajou.ac.kr

Abstract: In this study, we investigate tabs applied to turbulent flow over a circular cylinder for the reductions of the mean drag and lift fluctuations. Tabs are small and thin passive devices attached to the upper and lower surfaces of a circular cylinder near the flow separation. The Reynolds number considered is $Re = 3900$, based on the free-stream velocity and cylinder diameter. Large eddy simulations are performed using a dynamic global subgrid-scale eddy-viscosity model. A parametric study is carried out to find the optimal tab configuration for minimizing the mean drag and lift fluctuations. Parameters considered are the height (l_y) and width (l_z) of the tabs, and spanwise spacing (λ_z) between them. With the optimal parameters, the spanwise coherence of the vortex shedding behind the cylinder is effectively disrupted, resulting in three-dimensional vortical structures varying in the spanwise direction. As a result, the strength of the vortex shedding in the wake is successfully weakened, and the mean drag and lift fluctuations are significantly reduced by 14% and 95%, respectively, with the optimal tab configuration of $l_y/d = 0.2$, $l_z/d = 0.3$, and $\lambda_z/d = 4$, where d is the cylinder diameter.

Keywords: flow control; turbulent flow; flow over a cylinder; drag; lift; passive control

MSC: 76D55



Citation: Seo, J.; Yun, J.; Lee, J. Control of Turbulent Flow over a Circular Cylinder Using Tabs. *Mathematics* **2023**, *11*, 968. <https://doi.org/10.3390/math11040968>

Academic Editor: Smirnov Nikolay Nikolaevich

Received: 17 January 2023

Revised: 10 February 2023

Accepted: 11 February 2023

Published: 14 February 2023



Copyright: © 2023 by the authors. Licensee MDPI, Basel, Switzerland. This article is an open access article distributed under the terms and conditions of the Creative Commons Attribution (CC BY) license (<https://creativecommons.org/licenses/by/4.0/>).

1. Introduction

Unsteady flows past bluff bodies exhibit large-scale vortical structures such as the Kármán vortex shedding. The Kármán vortex significantly contributes to the mean drag and lift fluctuations, and also causes flow-induced vibrations and noise. Therefore, many researchers have proposed numerous control methods to suppress the strength of the Kármán vortex shedding [1–10]. In particular, flow over a circular cylinder is featured by the nominally two-dimensional distinct Kármán vortex shedding, and thus it has been the focus of extensive research on the flow control. According to Choi et al. [1], control methods for flow over a circular cylinder can be divided into two-dimensional (2D) and three-dimensional (3D) forcings based on whether or not actuations or geometric modifications for the control vary in the spanwise direction.

The control of flow over a circular cylinder with 2D forcing is a method in which actuations or geometric modifications are uniform along the spanwise direction. Examples for passive control devices in 2D forcing are the end plate [4,11], splitter plate [2,12–14], flexible splitter plate [15], secondary small cylinder [16–18], and so on. Active control strategies categorized in 2D forcing include the base bleed [3,5], steady and time-periodic blowing [9], and active feedback control with blowing/suction on the surface [6,8,10], to name a few. These control methods have been shown to successfully weaken the strength of the Kármán vortex shedding in the wake of the cylinder. For example, recent work by Yun and Lee [10] performed an active feedback control of turbulent flow over a circular cylinder at $Re = 3900$, where the amplitude of the uniform blowing/suction actuation near the flow separation is linearly proportional to the averaged transverse velocity at a sensing location on the centerplane of the wake. Here, the Reynolds number ($Re = u_\infty d/\nu$) is defined with the free-stream velocity (u_∞), the cylinder diameter (d), and the kinematic viscosity (ν).

They showed that, with the control, the vortex shedding behind the cylinder was weakened and delayed farther downstream, resulting in the reductions of the mean drag and lift fluctuations on the cylinder.

On the other hand, the control of flow over a circular cylinder with 3D forcing employs actuations or geometric modifications varying in the spanwise direction, which is intended to disturb the spanwise coherence of the vortex shedding in the wake. One of the representative control methods in 3D forcing is the distributed forcing proposed by Kim and Choi [7]. They installed blowing and suction actuations on the upper and lower slots of the cylinder surface near the flow separation, which were steady in time and distributed in the spanwise direction with a sinusoidal profile. They showed that this distributed forcing effectively disrupted the formation of the Kármán vortex shedding in the wake, and thus resulted in the reductions of the mean drag and lift fluctuations. Active open-loop control with the distributed forcing has an advantage that its control efficiency is much better than other active open-loop controls using 2D forcing, such as the base bleed or the steady and time-periodic blowing [1,9].

Controls with 3D forcing can also be accomplished with passive devices that introduce geometric modifications of the cylinder varying in the spanwise direction. Passive devices in 3D forcing include trailing edge [19–21], wavy cylinder [22,23], O-ring [24], helically twisted elliptic (HTE) cylinder [25,26], and so on. For example, the HTE cylinder has an elliptic cross section that rotates along the spanwise axis of the cylinder, and Kim et al. [26] conducted an extensive parametric study for the optimal shape of the HTE cylinder for both laminar and turbulent flow regimes. For Reynolds numbers considered in their study, it was reported that both the drag and lift fluctuations for the optimal HTE cylinders were smaller than those for a circular cylinder. In their study, the optimal spanwise wavelength of the HTE cylinder for the maximum drag reduction was around $3d \sim 5d$, and this was consistent with that of the distributed forcing. Unlike active controls, these passive devices are attractive because they do not require any power consumption for active actuations. Nevertheless, these passive devices require substantial geometric modifications to bluff bodies, and thus it may be difficult to apply them to some apparatuses having bluff body shapes.

In contrast, tabs [27–30] can be attached to a bluff body without a significant geometric modification of its shape, and thus they can be readily applied to the control of flow over a bluff body. Park et al. [29] carried out an extensive parametric study for the effects of the height and width of tabs, and the spanwise spacing between adjacent tabs on the drag reduction of two-dimensional bluff body with a blunt trailing edge in turbulent flow. Through both experimental and numerical approaches, they showed that tabs attached to the upper and lower trailing edges of the bluff body effectively caused spanwise variations of vortical structures in the wake weakening the two-dimensional nature of the vortex shedding. As a result, it was observed that the base pressure of the bluff body was increased owing to the tabs. Later, Park et al. [30] showed that tabs attached to backward facing step could also be used for the mixing enhancement. In their work, tabs were found to significantly disturb the separating shear layer by generating a pair of counter-rotating streamwise vortices, which entrained high momentum fluids into the recirculation region behind the backward-facing step, greatly improving the flow mixing. On the other hand, Yoon et al. [28] investigated tabs attached to a circular cylinder where the separation location is movable unlike a body with a blunt trailing edge. At the Reynolds number of 100, the laminar flow behind a circular cylinder is successfully controlled by tabs, resulting in the suppression of the Kármán vortex shedding and the drag reduction of 17%. However, for turbulent flow over a circular cylinder, the applicability of tabs for the reductions of the mean drag and lift fluctuations has not yet been investigated in literature. Therefore, this study aims to investigate the use of tabs for controlling turbulent flow over a circular cylinder and examine their effectiveness in reducing the mean drag and lift fluctuations. The structure of this article is as follows: the numerical configurations and the

geometry of tabs are described in Section 2. The control results are presented and discussed in Section 3, followed by the conclusions in Section 4.

2. Numerical Configurations

In the present study, we conduct large eddy simulations (LES) of turbulent flows over a circular cylinder with or without tabs. The governing equations for this flow are the unsteady incompressible filtered continuity and Navier–Stokes equations:

$$\frac{\partial \bar{u}_j}{\partial x_j} - q = 0, \tag{1}$$

and

$$\frac{\partial \bar{u}_i}{\partial t} + \frac{\partial \bar{u}_i \bar{u}_j}{\partial x_j} = -\frac{\partial \bar{p}}{\partial x_i} + \frac{1}{Re} \frac{\partial^2 \bar{u}_i}{\partial x_j \partial x_j} - \frac{\partial}{\partial x_j} \tau_{ij} + f_i, \tag{2}$$

where t is the time, $x_i = (x, y, z)$ are the Cartesian coordinates, $u_i = (u, v, w)$ are the corresponding velocity components, and p is the pressure. Here, x , y , and z denote the streamwise, transverse, and spanwise directions, respectively (see Figure 1). $\bar{(\)}$ denotes the filtering operation for LES. To satisfy the no-slip condition on the cylinder surface and tabs, we adopt an immersed boundary method by Kim et al. [31]. q and f_i in Equations (1) and (2) are the mass source/sink and momentum forcing terms to satisfy the continuity and the no-slip condition on the cylinder surface, respectively. These terms are only applied on the cylinder surface or inside the cylinder body and are set to be zero in other regions of fluid flow. The algorithms to determine q and f_i are described in Kim et al. [31]. Variables in Equations (1) and (2) are non-dimensionalized by the free-stream velocity u_∞ and the cylinder diameter d . $\tau_{ij} = \bar{u_i u_j} - \bar{u}_i \bar{u}_j$ is the subgrid-scale stress tensor for LES. The Reynolds number considered in this study is $Re = 3900$.

In the present study, we use the dynamic global subgrid-scale (SGS) eddy-viscosity model based on the Germano identity [32,33] to determine the subgrid-scale stress τ_{ij} for LES. The eddy viscosity model for τ_{ij} is written in the following form:

$$\tau_{ij} - \frac{1}{3} \tau_{kk} \delta_{ij} = -2\nu_T \bar{S}_{ij}, \tag{3}$$

$$\bar{S}_{ij} = \frac{1}{2} \left(\frac{\partial \bar{u}_i}{\partial x_j} + \frac{\partial \bar{u}_j}{\partial x_i} \right), \tag{4}$$

where ν_T is the subgrid-scale eddy viscosity, and \bar{S}_{ij} is the filtered strain rate tensor. ν_T is determined by the Vreman eddy viscosity model [34] in the following form:

$$\nu_T = C_v \sqrt{\frac{B_{\bar{\beta}}}{\bar{\alpha}_{ij} \bar{\alpha}_{ij}}}, \tag{5}$$

$$\bar{\alpha}_{ij} = \frac{\partial \bar{u}_j}{\partial x_i}, \tag{6}$$

$$B_{\bar{\beta}} = \bar{\beta}_{11} \bar{\beta}_{22} + \bar{\beta}_{11} \bar{\beta}_{33} + \bar{\beta}_{22} \bar{\beta}_{33} - \bar{\beta}_{12}^2 - \bar{\beta}_{13}^2 - \bar{\beta}_{23}^2, \tag{7}$$

$$\bar{\beta}_{ij} = \sum_{m=1}^3 \bar{\Delta}_m^2 \bar{\alpha}_{mi} \bar{\alpha}_{mj}, \tag{8}$$

where C_v is the Vreman model coefficient, and $\bar{\Delta}$ is the size of the grid filter. This model coefficient C_v is dynamically determined using the Germano identity [33,35] as follows:

$$C_v = -\frac{1}{2} \frac{\langle L_{ij} M_{ij} \rangle_V}{\langle M_{ij} M_{ij} \rangle_V}, \tag{9}$$

$$L_{ij} = \widetilde{\bar{u}_i \bar{u}_j} - \widetilde{\bar{u}_i} \widetilde{\bar{u}_j}, \tag{10}$$

$$M_{ij} = \sqrt{\frac{B_{\beta}}{\widetilde{\alpha_{ij}} \widetilde{\alpha_{ij}}} \widetilde{S}_{ij}} - \sqrt{\frac{B_{\beta}}{\bar{\alpha}_{ij} \bar{\alpha}_{ij}} \bar{S}_{ij}}, \tag{11}$$

where $\widetilde{(\cdot)}$ is the test-filtering operation, and $\langle \bullet \rangle_V$ is the instantaneous volume average over the entire computational domain. Owing to this volume averaging process, C_v is constant in the space but varies over time.

Inserting the eddy viscosity model in Equation (3) into the Navier–Stokes equation in Equation (2) gives

$$\frac{\partial \bar{u}_i}{\partial t} + \frac{\partial \bar{u}_i \bar{u}_j}{\partial x_j} = -\frac{\partial \bar{p}}{\partial x_i} + \frac{1}{Re} \frac{\partial^2 \bar{u}_i}{\partial x_j \partial x_j} + \frac{\partial}{\partial x_j} \nu_T \frac{\partial \bar{u}_i}{\partial x_j} + \frac{\partial}{\partial x_j} \nu_T \frac{\partial \bar{u}_j}{\partial x_i} + f_i. \tag{12}$$

Note that τ_{kk} in Equation (3) is merged into the pressure term [36]. For the time advancement of the Navier–Stokes equation, we use the fully implicit fractional step method with a velocity decoupling procedure [37–39]. By conducting a temporal integration using the second-order implicit Crank–Nicolson scheme together with a linearization of the nonlinear convection term preserving the second-order temporal accuracy by Beam and Warming [40],

$$u_i^{n+1} u_j^{n+1} + u_i^n u_j^n = u_i^{n+1} u_j^n + u_i^n u_j^{n+1} + O(\Delta t^2), \tag{13}$$

Equation (12) becomes

$$\begin{aligned} \frac{\bar{u}_i^{n+1} - \bar{u}_i^n}{\Delta t} + \frac{1}{2} \left(\frac{\partial}{\partial x_j} \bar{u}_j^n \bar{u}_i^{n+1} + \frac{\partial}{\partial x_j} \bar{u}_i^n \bar{u}_j^{n+1} \right) &= -\frac{\partial \bar{p}^{n+1}}{\partial x_i} + \frac{1}{2} \frac{1}{Re} \left(\frac{\partial^2 \bar{u}_i^{n+1}}{\partial x_j \partial x_j} + \frac{\partial^2 \bar{u}_i^n}{\partial x_j \partial x_j} \right) \\ &+ \frac{1}{2} \left(\frac{\partial}{\partial x_j} \nu_T \frac{\partial \bar{u}_i^{n+1}}{\partial x_j} + \frac{\partial}{\partial x_j} \nu_T \frac{\partial \bar{u}_i^n}{\partial x_j} \right) + \frac{1}{2} \left(\frac{\partial}{\partial x_j} \nu_T \frac{\partial \bar{u}_j^{n+1}}{\partial x_i} + \frac{\partial}{\partial x_j} \nu_T \frac{\partial \bar{u}_j^n}{\partial x_i} \right) + f_i. \end{aligned} \tag{14}$$

By introducing the intermediate velocity \bar{u}_i^* for the fractional step method [37–39], an equation for the intermediate velocity can be written as

$$\begin{aligned} \frac{\bar{u}_i^* - \bar{u}_i^n}{\Delta t} + \frac{1}{2} \left(\frac{\partial}{\partial x_j} \bar{u}_j^n \bar{u}_i^* + \frac{\partial}{\partial x_j} \bar{u}_i^n \bar{u}_j^* \right) &= -\frac{\partial \bar{p}^n}{\partial x_i} + \frac{1}{2} \frac{1}{Re} \left(\frac{\partial^2 \bar{u}_i^*}{\partial x_j \partial x_j} + \frac{\partial^2 \bar{u}_i^n}{\partial x_j \partial x_j} \right) \\ &+ \frac{1}{2} \left(\frac{\partial}{\partial x_j} \nu_T \frac{\partial \bar{u}_i^*}{\partial x_j} + \frac{\partial}{\partial x_j} \nu_T \frac{\partial \bar{u}_i^n}{\partial x_j} \right) + \frac{1}{2} \left(\frac{\partial}{\partial x_j} \nu_T \frac{\partial \bar{u}_j^*}{\partial x_i} + \frac{\partial}{\partial x_j} \nu_T \frac{\partial \bar{u}_j^n}{\partial x_i} \right) + f_i. \end{aligned} \tag{15}$$

By defining the delta form $\delta\bar{u}_i^* = \bar{u}_i^* - \bar{u}_i^n$ and substituting it to Equation (15), we can obtain an equation for $\delta\bar{u}_i^*$:

$$\begin{aligned} & \frac{\delta\bar{u}_i^*}{\Delta t} + \frac{1}{2} \left(\frac{\partial}{\partial x_j} \bar{u}_j^n (\bar{u}_i^n + \delta\bar{u}_i^*) + \frac{\partial}{\partial x_j} \bar{u}_i^n (\bar{u}_j^n + \delta\bar{u}_j^*) \right) \\ &= -\frac{\partial \bar{p}^n}{\partial x_i} + \frac{1}{2} \frac{1}{Re} \left(\frac{\partial^2}{\partial x_j \partial x_j} (\bar{u}_i^n + \delta\bar{u}_i^*) + \frac{\partial^2 \bar{u}_i^n}{\partial x_j \partial x_j} \right) \\ & \quad + \frac{1}{2} \left(\frac{\partial}{\partial x_j} \nu_T \frac{\partial}{\partial x_j} (\bar{u}_i^n + \delta\bar{u}_i^*) + \frac{\partial}{\partial x_j} \nu_T \frac{\partial \bar{u}_i^n}{\partial x_j} \right) \\ & \quad + \frac{1}{2} \left(\frac{\partial}{\partial x_j} \nu_T \frac{\partial}{\partial x_i} (\bar{u}_j^n + \delta\bar{u}_j^*) + \frac{\partial}{\partial x_j} \nu_T \frac{\partial \bar{u}_j^n}{\partial x_i} \right) + f_i. \end{aligned} \tag{16}$$

By rearranging Equation (16),

$$\begin{aligned} & \frac{\delta\bar{u}_i^*}{\Delta t} + \frac{1}{2} \frac{\partial}{\partial x_j} \bar{u}_i^n \delta\bar{u}_j^* + \frac{1}{2} \frac{\partial}{\partial x_j} \bar{u}_j^n \delta\bar{u}_i^* - \frac{1}{2Re} \frac{\partial^2 \delta\bar{u}_i^*}{\partial x_j \partial x_j} - \frac{1}{2} \frac{\partial}{\partial x_j} \nu_T \frac{\partial \delta\bar{u}_i^*}{\partial x_j} - \frac{1}{2} \frac{\partial}{\partial x_j} \nu_T \frac{\partial \delta\bar{u}_j^*}{\partial x_i} \\ &= -\frac{\partial \bar{p}^n}{\partial x_i} - \frac{\partial}{\partial x_j} \bar{u}_i^n \bar{u}_j^n + \frac{1}{Re} \frac{\partial^2 \bar{u}_i^n}{\partial x_j \partial x_j} + \frac{\partial}{\partial x_j} \nu_T \frac{\partial \bar{u}_i^n}{\partial x_j} + \frac{\partial}{\partial x_j} \nu_T \frac{\partial \bar{u}_j^n}{\partial x_i} + f_i. \end{aligned} \tag{17}$$

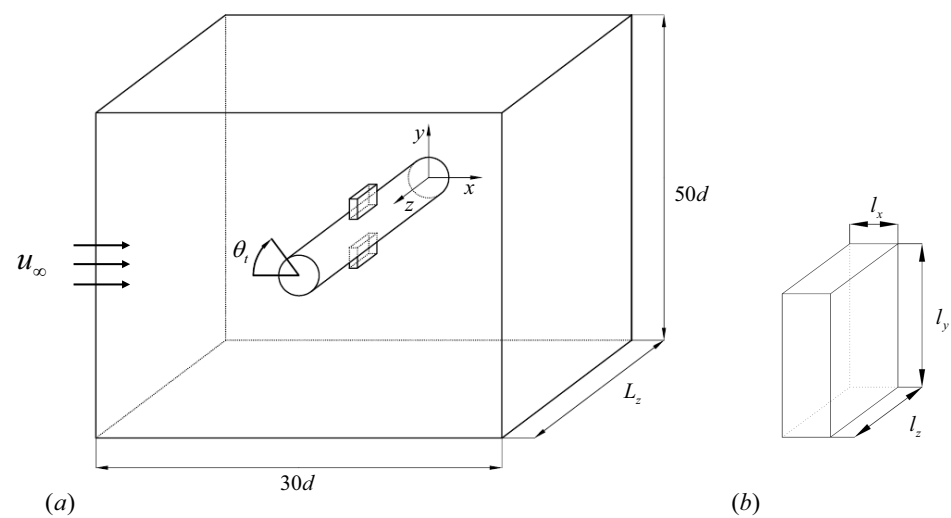


Figure 1. (a) Schematic diagram for the coordinate system, computational domain, and geometry of a circular cylinder with tabs; (b) geometric parameters of tab thickness (l_x), height (l_y), and width (l_z).

Equation (17) can be expressed in a matrix form

$$\frac{1}{\Delta t} \begin{pmatrix} I + \Delta t N_{11} & \Delta t N_{12} & \Delta t N_{13} \\ \Delta t N_{21} & I + \Delta t N_{22} & \Delta t N_{23} \\ \Delta t N_{31} & \Delta t N_{32} & I + \Delta t N_{33} \end{pmatrix} \begin{pmatrix} \delta\bar{u}_1^* \\ \delta\bar{u}_2^* \\ \delta\bar{u}_3^* \end{pmatrix} = \begin{pmatrix} R_1 \\ R_2 \\ R_3 \end{pmatrix}, \tag{18}$$

where R_i denotes the right-hand-side of Equation (17). Here, N_{ij} is given as

$$N_{ij} = \begin{cases} \frac{1}{2} \frac{\partial}{\partial x_j} (\bar{u}_i^n + \bar{u}_j^n) - \frac{1}{2Re} \frac{\partial^2}{\partial x_j \partial x_j} - \frac{1}{2} \frac{\partial}{\partial x_j} \nu_T \left(\frac{\partial}{\partial x_i} + \frac{\partial}{\partial x_j} \right) & (i = j) \\ \frac{1}{2} \frac{\partial}{\partial x_j} \bar{u}_i^n - \frac{1}{2} \frac{\partial}{\partial x_j} \nu_T \frac{\partial}{\partial x_i} & (i \neq j). \end{cases} \tag{19}$$

While preserving the second-order temporal accuracy, we carry out the approximate factorization of the coefficient matrix in Equation (18), which gives [39]

$$\frac{1}{\Delta t} \begin{pmatrix} I + \Delta t N_{11} & 0 & 0 \\ \Delta t N_{21} & I + \Delta t N_{22} & 0 \\ \Delta t N_{31} & \Delta t N_{32} & I + \Delta t N_{33} \end{pmatrix} \begin{pmatrix} I & \Delta t N_{12} & \Delta t N_{13} \\ 0 & I & \Delta t N_{23} \\ 0 & 0 & I \end{pmatrix} \begin{pmatrix} \delta \bar{u}_1^* \\ \delta \bar{u}_2^* \\ \delta \bar{u}_3^* \end{pmatrix} = \begin{pmatrix} R_1 \\ R_2 \\ R_3 \end{pmatrix}. \quad (20)$$

After calculating $\delta \bar{u}_i^*$ from the above equation without iterations, we can subsequently obtain \bar{p}^{n+1} and \bar{u}_i^{n+1} . More details on this implicit velocity decoupling procedure for the incompressible Navier–Stokes equations are referred to Kim et al. [39]. For the discretization of spatial derivative terms in the Navier–Stokes equation, we adopt the second-order central difference scheme for all spatial derivative terms except for the convection terms in the laminar accelerating region near the cylinder where a third-order QUICK scheme is employed [41]. In this study, simulations are carried out using in-house code implementing the above numerical configurations. The code has been demonstrated to accurately predict turbulent flows over various bluff bodies [32,41,42].

Figure 1 shows the schematic diagram for the coordinate system, computational domain, and geometry of a circular cylinder with tabs. At the inflow boundary, a Dirichlet boundary condition, $u = u_\infty$ and $v = w = 0$, is applied. A periodic boundary condition is used in the spanwise direction and $\partial u / \partial y = v = \partial w / \partial y = 0$ is given at the top and bottom boundaries. At the outflow boundary, a convective boundary condition is given as $\partial u_i / \partial t + c \partial u_i / \partial x = 0$, where c is the plane-averaged streamwise velocity on the outflow plane. The computational domain for the present numerical simulations is $-15 \leq x/d \leq 15$, $-25 \leq y/d \leq 25$, and $0 \leq z/d \leq L_z$, where L_z is dependent on the spanwise distance between adjacent tabs (λ_z) (see Table 1). $L_z/d = 4$ is used for the LES of flow over a circular cylinder without a tab.

Table 1. Geometric parameters of the tabs, computational domain sizes, and numbers of grid points.

| l_y/d | l_z/d | λ_z/d | Domain Size ($L_x \times L_y \times L_z$) | Number of Grid Points ($N_x \times N_y \times N_z$) |
|---------|---------|---------------|--|---|
| 0.2 | 0.1 | 4 | $30d \times 50d \times 4d$ | $513 \times 331 \times 160$ |
| | 0.2 | | | |
| | 0.3 | | | |
| | 0.4 | | | |
| | 0.5 | | | |
| 0.3 | 0.1 | | | |
| | 0.2 | | | |
| | 0.3 | | | |
| | 0.4 | | | |
| | 0.5 | | | |
| 0.4 | 0.1 | | | |
| | 0.2 | | | |
| | 0.3 | | | |
| | 0.4 | | | |
| | 0.5 | | | |
| 0.2 | 0.3 | 2 | $30d \times 50d \times 2d$ | $513 \times 331 \times 80$ |
| | | 3 | $30d \times 50d \times 3d$ | $513 \times 331 \times 120$ |
| | | 5 | $30d \times 50d \times 5d$ | $513 \times 331 \times 200$ |
| | | 6 | $30d \times 50d \times 6d$ | $513 \times 331 \times 240$ |

In Figures 1 and 2, there are five geometric parameters for tabs: the installation angle of tabs measured from the stagnation point (θ_t), thickness (l_x), height (l_y), width (l_z), and spanwise distance between adjacent tabs (λ_z). Yoon et al. [28] investigated the effect of θ_t for flow over a circular cylinder at the low Reynolds number of $Re = 100$, and showed that $\theta_t = 90^\circ$ (see Figure 1a) is the optimal location of tabs for the reduction of the mean

drag on the cylinder. Therefore, in this study, we install tabs at $\theta_t = 90^\circ$. The separation angle for flow over a cylinder at $Re = 3900$ from the present LES is $\theta_s = 89^\circ$, which is in good agreement with those from other investigations [43,44]. Thus, the installation location of tabs ($\theta_t = 90^\circ$) is near the flow separation. Figure 2 shows an example of a circular cylinder attached by multiple tabs installed at $\theta_t = 90^\circ$ with the free-stream velocity u_∞ . Most studies on tabs attached to bluff bodies adopt tabs having a thin thickness [28–30]. Accordingly, the present study also assumes a thin tab with the thickness of $l_x = 0.04d$ [28]. Previous studies on the control of flow over a circular cylinder with 3D forcing reported that the optimal spanwise wavelength for various 3D forcing methods for the drag reduction is around $4d$ [7,26,28]. In particular, through a parametric study, Yoon et al. [28] showed that $\lambda_z/d = 4$ is the optimal spanwise distance for tabs in the laminar flow over a circular cylinder. Therefore, with the fixed spanwise distance of $\lambda_z/d = 4$, this study focuses on a parametric study by varying the tab height (l_y) and width (l_z). In addition, we examine the effect of spanwise distance of tabs (λ_z) as well.

Table 1 shows geometric parameters for tabs, computational domain sizes, and numbers of grid points considered in the present study. As shown, we consider $0.2 \leq l_y/d \leq 0.4$ and $0.1 \leq l_z/d \leq 0.5$. The streamwise and transverse domain sizes are $L_x = 30d$ and $L_y = 50d$ and corresponding numbers of grid points are $N_x = 513$ and $N_y = 331$. The spanwise domain size and number of spanwise grid points depend on the size of λ_z . That is, $L_z = \lambda_z$ and $N_z = 40\lambda_z/d$. Tabs are installed at $z = L_z/2$. Figure 3 shows grid distributions near a circular cylinder with tabs in the x - y plane. As shown, with the adoption of the immersed boundary method [31], grid lines and the geometry of a circular cylinder with tabs are not aligned with each other. Simulations with a larger number of grid points give negligible changes in flow statistics confirming the numerical accuracy of the present study. For the present unsteady simulations, the size of computational time step is determined from a maximum CFL number condition, $CFL = \Delta t(|u|\Delta x + |v|\Delta y + |w|\Delta z) \leq 0.7$. Simulations with different maximum CFL number conditions such as $CFL \leq 0.525$ do not result in changes to the flow statistics, indicating that the effect of computational time step is negligible [45–47].

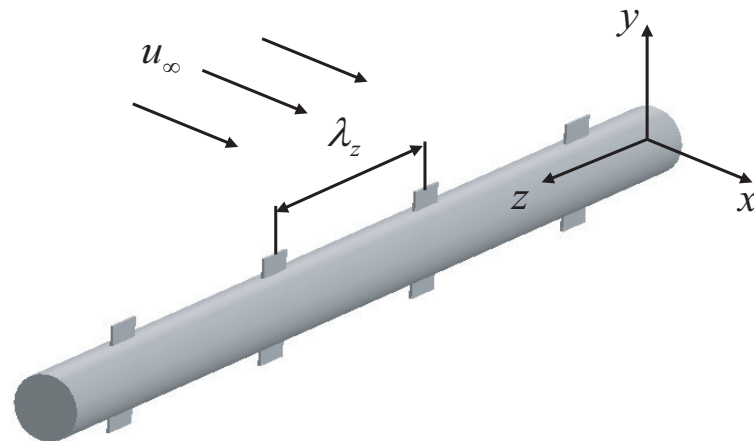


Figure 2. Schematic diagram of a circular cylinder attached by multiple tabs installed at $\theta_t = 90^\circ$ with the free-stream velocity u_∞ . λ_z denotes the spanwise distance between adjacent tabs.

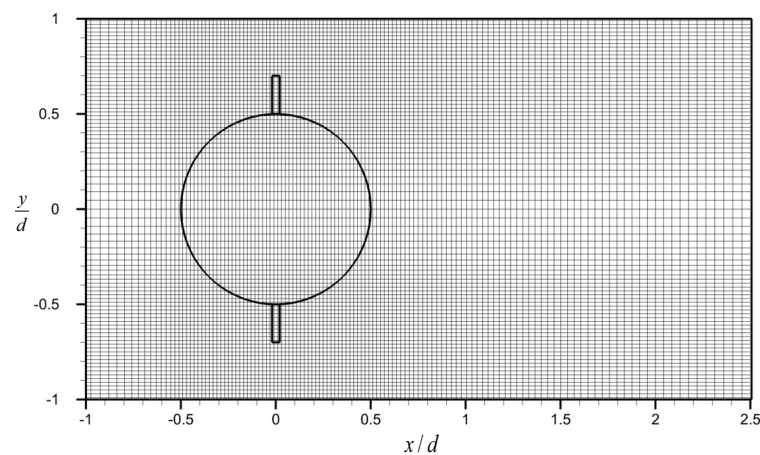


Figure 3. Grid distributions near a circular cylinder with tabs in the x - y plane. Every other grid is shown.

3. Results and Discussion

3.1. Control Results

Table 2 shows the flow statistics for turbulent flow over a circular cylinder without a tab from the present LES together with those from previous studies. In the table, the mean drag coefficient (C_D), coefficient of lift fluctuations ($C_{L_{rms}}$), Strouhal number (St), mean recirculation length (L_r/d), and base pressure coefficient ($-C_{P_b}$) are shown. The mean recirculation length L_r is defined to be the length between the base of the cylinder ($x/d = 0.5$) and the point of zero mean streamwise velocity on the centerline ($y = 0$). The base pressure coefficient $-C_{P_b}$ is the pressure coefficient at the cylinder base ($x/d = 0.5$). As shown in Table 2, the flow statistics from the present LES agree well with those from the previous investigations.

Table 2. Flow statistics for turbulent flow over a circular cylinder without a tab from the present simulation together with those from previous studies. Here, DNS denotes direct numerical simulation.

| Case | Re | C_D | $C_{L_{rms}}$ | St | L_r/d | $-C_{P_b}$ |
|--------------------------------|------|-------|---------------|-------|---------|------------|
| Lehmkuhl et al. [44] (DNS) | 3900 | 1.015 | - | 0.215 | 1.36 | 0.935 |
| Kravchenko and Moin [43] (LES) | 3900 | 1.04 | - | 0.21 | 1.35 | 0.94 |
| Kim et al. [26] (LES) | 3900 | 1.05 | 0.25 | - | - | 0.98 |
| Lam et al. [48] (experiment) | 4000 | 1.03 | 0.16 | - | - | - |
| Lam et al. [48] (LES) | 3900 | 1.03 | 0.12 | 0.211 | - | - |
| Franke and Frank [49] (LES) | 3900 | 0.978 | - | 0.209 | 1.64 | 0.85 |
| Present study (LES) | 3900 | 1.045 | 0.18 | 0.208 | 1.38 | 0.91 |

Figure 4 shows the variations of drag and lift coefficients with the tab height (l_y) and width (l_z). Here, we fix $\lambda_z/d = 4$. As shown, tabs with $l_z/d \geq 0.2$ successfully reduce the mean drag and root-mean-square (rms) of lift fluctuations exerted on the cylinder. The maximum reductions of the mean drag and lift fluctuations are achieved with the tab size of $l_y/d = 0.2$ and $l_z/d = 0.3$, which correspond to about 14% ($C_D = 0.90$) and 95% ($C_{L_{rms}} = 0.0096$) reductions, respectively, compared to the values of the uncontrolled flow (flow over a circular cylinder without a tab). We note that these reductions for turbulent flow are similar to those for laminar flow over a circular cylinder [28]. Tabs larger than this optimal tab size ($l_y/d \geq 0.2$ and $l_z/d \geq 0.4$) also reduce the mean drag and lift fluctuations but to a lesser extent. We suspect that this is because the form drag exerted on the tabs themselves increases with increasing the tab size [28]. On the other hand, for the cases of cylinder with relatively small tabs of $l_z/d = 0.1$, the mean drag and lift fluctuations are not reduced compared to the case of cylinder without a tab, indicating that small tabs are not effective in altering the turbulent flow over a circular cylinder. Figure 5 shows the time

histories of drag and lift coefficients with and without tabs. As expected from Figure 4, a circular cylinder attached by the optimal size tabs experiences significantly reduced drag and lift fluctuations.

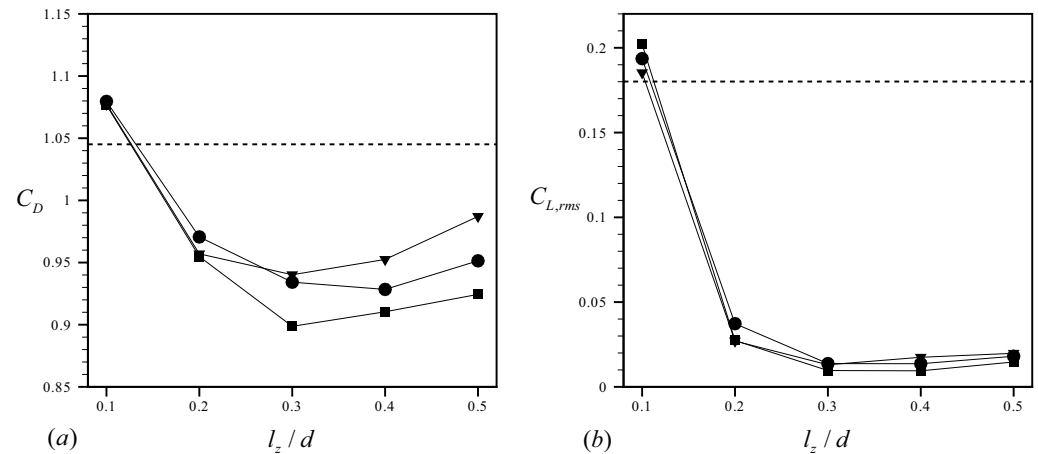


Figure 4. Variations of drag and lift coefficients with the tab height (l_y) and width (l_z) ($\lambda_z/d = 4$): (a) mean drag coefficient; (b) rms of lift coefficient. ■, $l_y/d = 0.2$; ●, $l_y/d = 0.3$; ▼, $l_y/d = 0.4$. Here, dashed lines denote values for the uncontrolled flow.

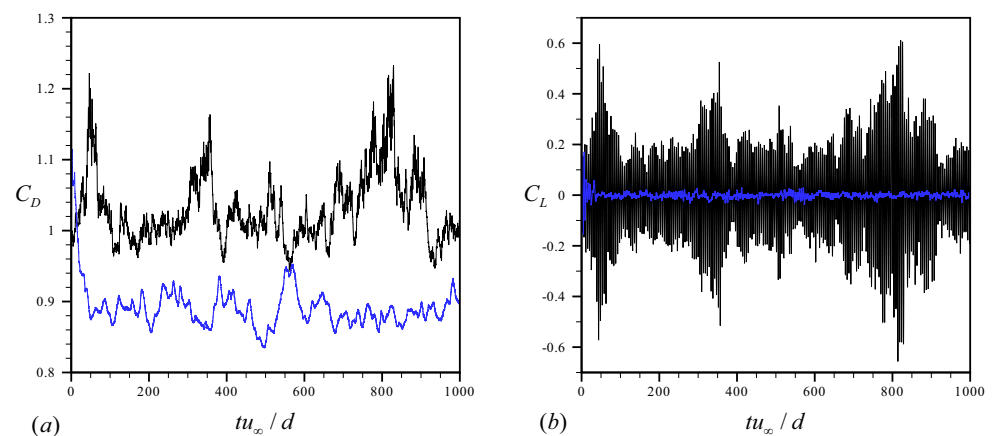


Figure 5. Time histories of drag and lift coefficients with and without tabs: (a) drag coefficient; (b) lift coefficient. Black line, cylinder without a tab; blue line, cylinder with tabs of $l_y/d = 0.2$ and $l_z/d = 0.3$.

Figure 6 shows the variations of drag and lift coefficients with the spanwise tab spacing λ_z . As shown, the optimal tab size of $l_y/d = 0.2$ and $l_z/d = 0.3$ obtained for $\lambda_z/d = 4$ again produces effective drag reductions for $3 \leq \lambda_z/d \leq 6$. In the figure, the optimal spanwise tab spacing is found to be $\lambda_z/d = 4$. For $\lambda_z/d = 2$, the drag increases owing to the close spacing between tabs. On the other hand, as shown in Figure 4b, the lift fluctuations are successfully reduced for all λ_z considered in this study. We note that the optimal spanwise tab spacing ($\lambda_z/d = 4$) in the present study is consistent with those of the previous investigations for 3D forcing such as the distributed forcing [7] and tabs in the laminar flow regime [28].

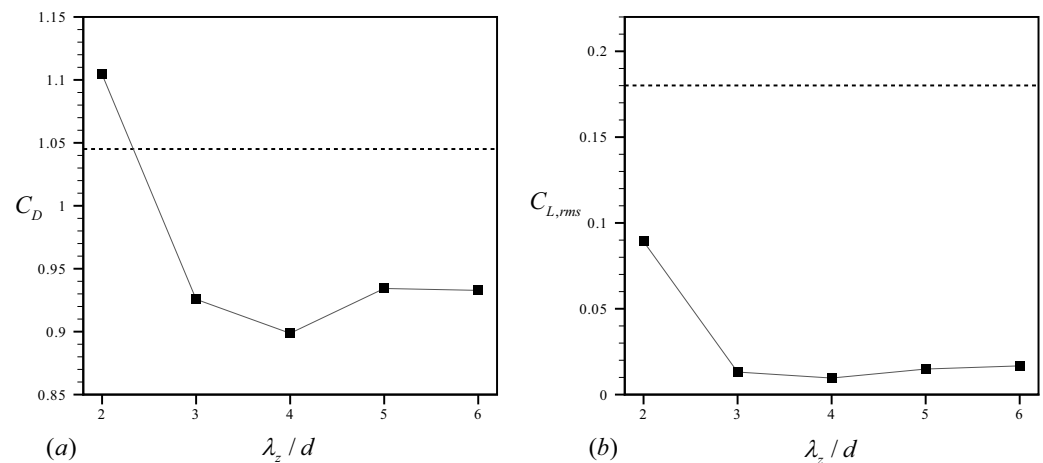


Figure 6. Variations of drag and lift coefficients with the spanwise tab spacing λ_z : (a) mean drag coefficient; (b) rms of lift coefficient. Here, we use the fixed tab size of $l_y = 0.2d$ and $l_z = 0.3d$, and dashed lines denote values for the uncontrolled flow.

3.2. Flow Fields

In the previous section, we examined that the control performance varies with the tab size (l_y and l_z) and spacing (λ_z), and showed that tabs with adequate sizes and spacings can effectively reduce the mean drag and lift fluctuations exerted on a circular cylinder. In this section, we elucidate flow fields modified by tabs with the optimal tab spacing of $\lambda_z/d = 4$.

Figure 7 shows instantaneous vortical structures over a circular cylinder with and without tabs identified using the λ_2 method [50] in top and side views. For the uncontrolled flow in Figure 7a,b, it is observed that wavy and asymmetric vortical structures are formed behind the cylinder owing to the development of the alternating Kármán vortex shedding. For the tabs of $l_y/d = 0.2$ and $l_z/d = 0.1$, vortical structures near tabs are slightly disrupted by tabs as shown in Figure 7c,d, but those in the wake exhibit wavy and asymmetric structures similar to those of the uncontrolled flow. This could explain the comparable values of drag and lift fluctuations for this size of tab to those of the uncontrolled flow. On the other hand, as shown in Figure 7f, the optimal tabs ($l_y/d = 0.2$ and $l_z/d = 0.3$) effectively weaken the alternating Kármán vortex shedding, resulting in symmetric vortical structures in the near wake with respect to the center plane ($y = 0$). In addition, vortices right behind the cylinder without a tab observed in Figure 7a become less prominent by tabs as shown in Figure 7e,f. These suppressions of vortices behind the cylinder and the vortex shedding are responsible for the significant reductions of the mean drag and lift fluctuations of the cylinder as observed in Figure 4.

Figure 8 shows instantaneous velocity vector fields on the x - z plane at $y/d = 0.6$ with and without tabs. For the case of optimal tabs, it is observed that the flow significantly is accelerated after the separation from the sides of the tab and vortices elongated in the streamwise direction are formed behind the tab. Similar elongated vortices were observed in other investigations with 3D forcing methods such as tabs in a body with a blunt trailing edge [29] and a helically-twisted-elliptic cylinder [25]. In contrast to the uncontrolled flow, these elongated vortices after tabs disrupt the coherence of the vortex shedding in the spanwise direction, transforming the nominally two-dimensional vortical structure into a three-dimensional one. This is a typical result of using 3D forcing methods [1].

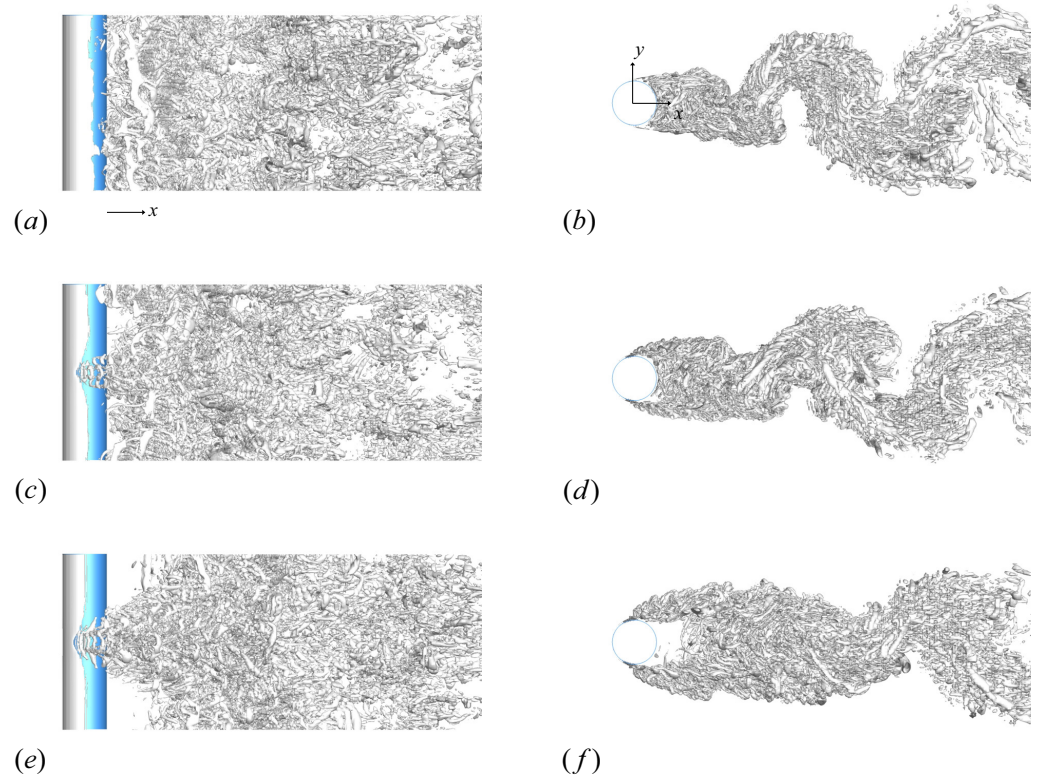


Figure 7. Instantaneous vortical structures over a circular cylinder with and without tabs identified using the λ_2 method [50] in top view (left) and in side view (right): (a,b) cylinder without a tab; (c,d) cylinder with tabs of $l_y/d = 0.2$ and $l_z/d = 0.1$; (e,f) cylinder with tabs of $l_y/d = 0.2$ and $l_z/d = 0.3$.

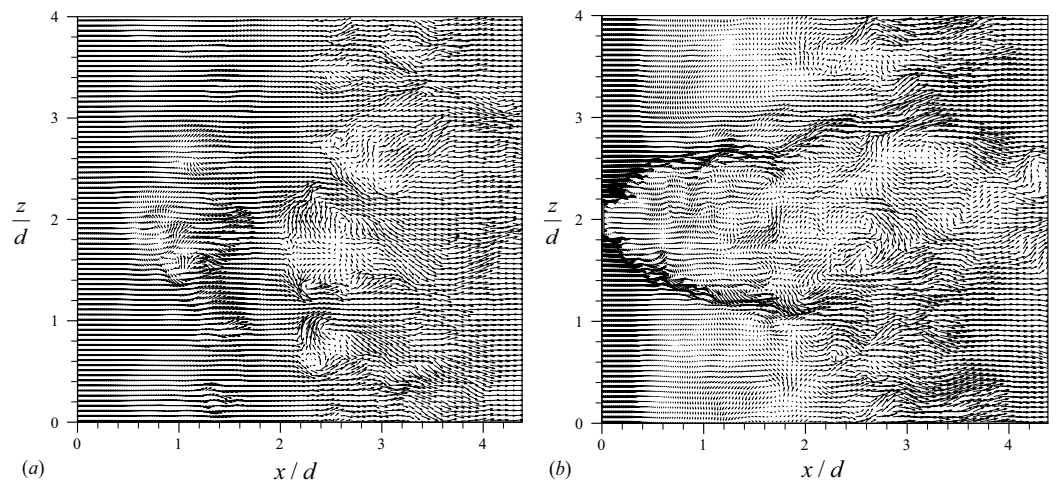


Figure 8. Instantaneous velocity vector fields on the x - z plane at $y/d = 0.6$: (a) cylinder without a tab; (b) cylinder with tabs of $l_y/d = 0.2$ and $l_z/d = 0.3$. Note that the x - z plane at $y/d = 0.6$ is located slightly above the cylinder.

The differences between two- and three-dimensional vortical structures can be observed by comparing Figure 7a,e. In Figure 7a, the flow structures in the wake for the uncontrolled flow are irregularly distributed along the spanwise direction without significant large-scale variations, resulting in a statistically homogeneous flow in that direction. On the other hand, in Figure 7e, the vortical structures in the wake modified by tabs exhibit evident large-scale variations along the spanwise direction owing to the elongated vortices

generated by tabs. Consequently, the flow is no longer statistically homogeneous in the spanwise direction.

To obtain another look at three-dimensional vortical structures, we draw instantaneous spanwise vorticity (ω_z) contours over a circular cylinder with and without tabs on x - y planes in Figure 9. The uncontrolled flow in Figure 9a shows the flow separation, evolution and roll-up of the shear layer, and vortex shedding in the wake. In contrast, for the flow with tabs, the roll-up of the shear layer on the x - y plane at $z/d = 0$ (as shown in Figure 9b) takes place farther downstream compared to the roll-up in the uncontrolled flow. On the other hand, in the vorticity contour on $z/d = 2$ with tabs (as shown in Figure 9c), the shear layers evolve at higher transverse locations after the flow separation at the tab tips. These distinct differences of vortical structures in the wake between those right behind the tab ($z/d = 2$) and those between tabs ($z/d = 0$) clearly indicate the formation of the three-dimensional vortical structures varying in the spanwise direction owing to the tabs. Thus far, we have examined the three-dimensionality of vortical structures behind a cylinder with tabs using the λ_2 method and vorticity (ω_z) fields. In addition to these methods, we note that analyses adopting other vortex identification approaches such as Lagrangian coherent structures [51–54] would be an interesting topic of exploration for future research.

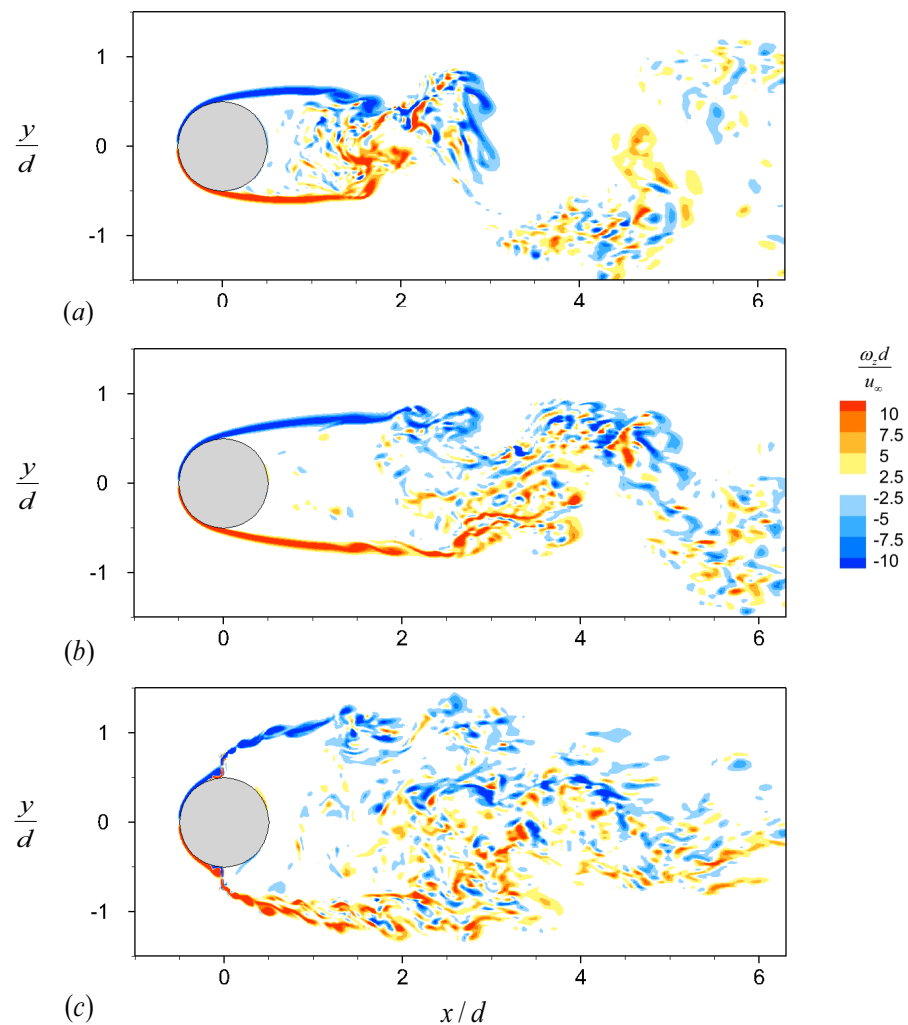


Figure 9. Instantaneous spanwise vorticity (ω_z) contours over a circular cylinder with and without tabs on x - y planes: (a) cylinder without a tab; (b,c) cylinder with tabs of $l_y/d = 0.2$ and $l_z/d = 0.3$. x - y planes for (b,c) are $z/d = 0$ and $z/d = 2$, respectively. For (b,c), note that tabs are located at $z/d = 2$.

Figure 10 depicts instantaneous pressure contours over a circular cylinder with and without tabs on x - y planes. For the uncontrolled flow shown in Figure 10a, it is apparent that a distinct low pressure region exists around $x/d = 1.6$ in the wake. However, as shown in Figure 10b,c, for the flow with tabs, this low pressure region disappears in the wake, and the pressure on the rear surface of the cylinder is recovered compared to that for the uncontrolled flow, resulting in the drag reduction. This behavior of pressure recovery on the cylinder base is again observed in Figure 11, which display instantaneous pressure contours of flow over a circular cylinder with and without tabs on the centerplane ($y = 0$) in the wake. In addition, in Figure 10a, a clear pressure difference between the top and bottom surfaces of the cylinder is observed in the case without a tab, but this pressure difference is alleviated with tabs (Figure 10b,c) causing the significant attenuation of lift fluctuations.

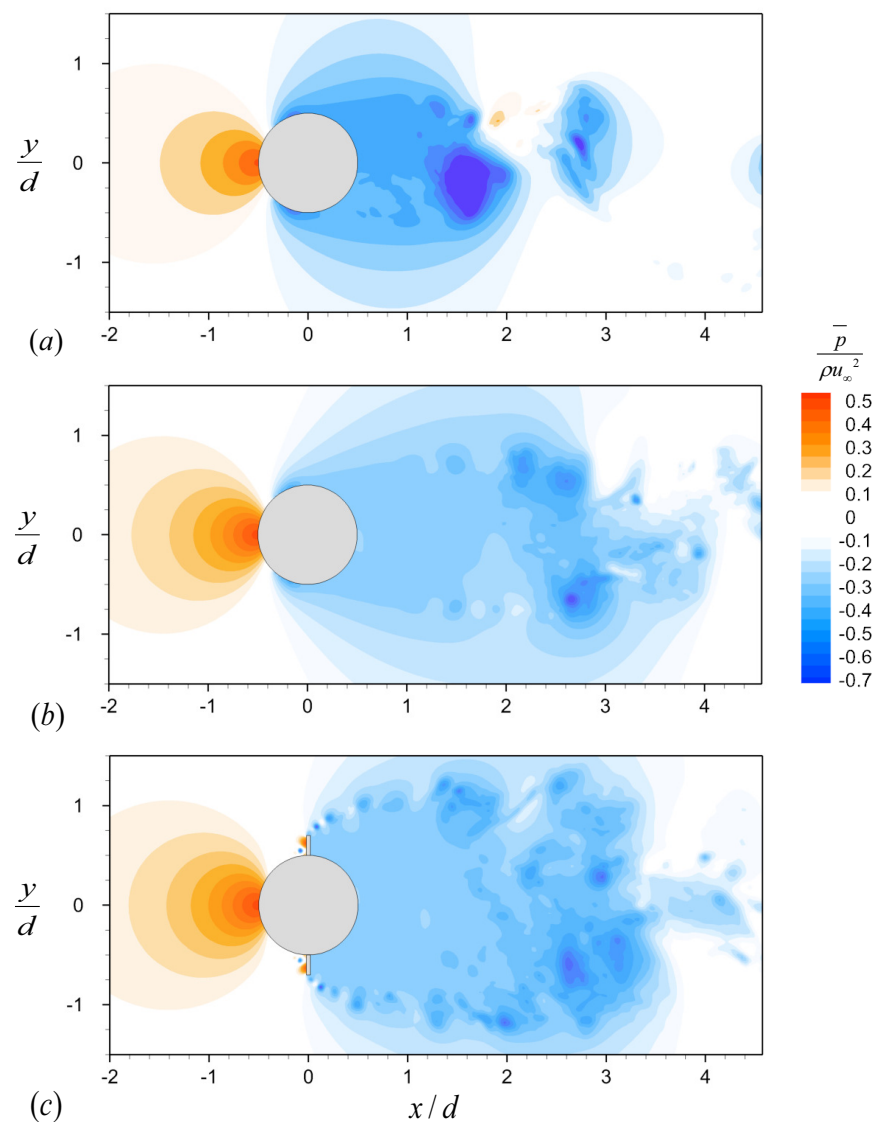


Figure 10. Instantaneous pressure contours over a circular cylinder with and without tabs on x - y planes. Details for (a–c) are the same as in the caption of Figure 9. In addition, the temporal instances for (a–c) are identical to those in Figure 9.

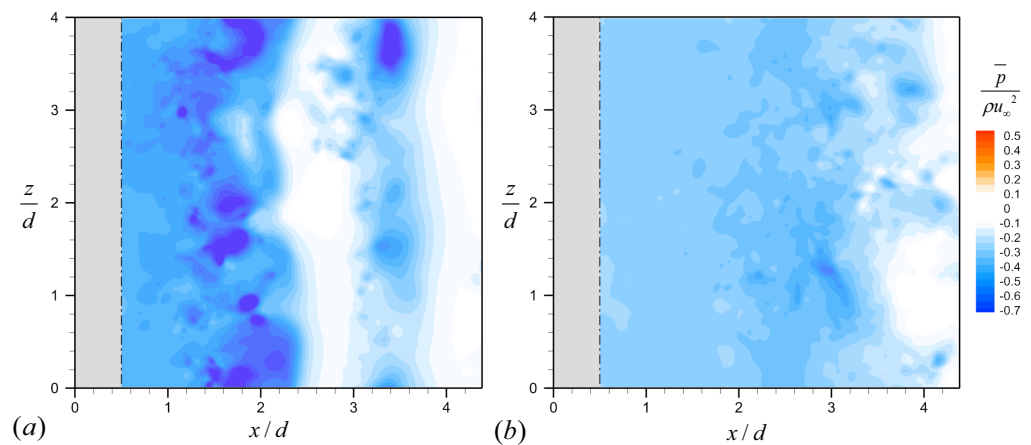


Figure 11. Instantaneous pressure contours of flow over a circular cylinder with and without tabs on the centerplane ($y = 0$) in the wake: (a) cylinder without a tab; (b) cylinder with tabs of $l_y/d = 0.2$ and $l_z/d = 0.3$.

Figure 12a shows the spanwise variations of the mean base pressure coefficient (C_{p_b}). Compared to the mean base pressure $C_{p_b} = -0.91$ of the uncontrolled flow, it is observed that tabs significantly increase the mean base pressure of the cylinder ($C_{p_b} = -0.61$), resulting in the reduction of mean drag. Figure 12b shows the spanwise variations of recirculation length in the wake. The recirculation length for the uncontrolled flow is $L_r/d = 1.38$, which agrees well with those of the previous studies in Table 2. With the optimal tabs of $l_y/d = 0.2$ and $l_z/d = 0.3$, the recirculation length is significantly increased for all spanwise locations, which is favorable to the drag reduction of bluff bodies [1,26,55].

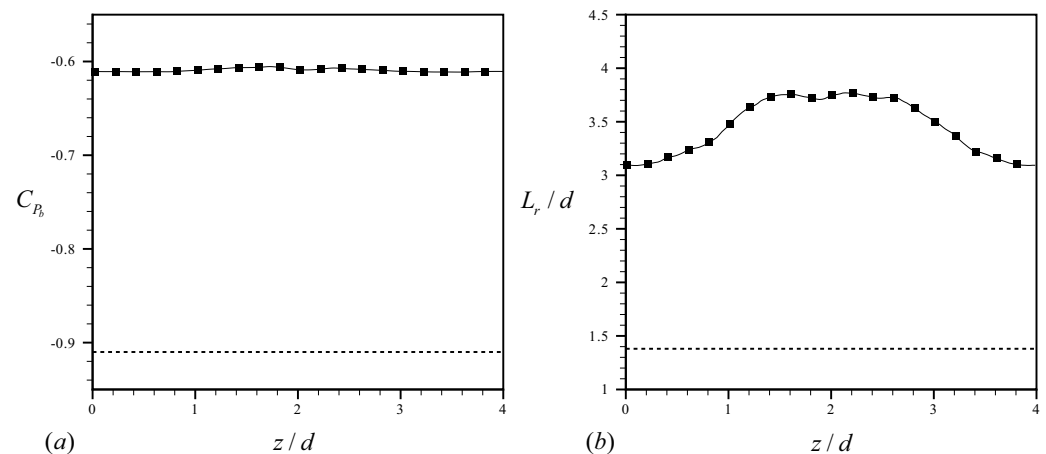


Figure 12. Spanwise variations of the mean base pressure coefficient (C_{p_b}) and recirculation length in the wake (L_r): (a) C_{p_b} ; (b) L_r/d . Dashed line, cylinder without a tab; —■— cylinder with tabs of $l_y/d = 0.2$ and $l_z/d = 0.3$.

Figure 13 shows the mean square of transverse velocity fluctuations and mean streamwise velocity at $x/d = 1.06$ and $x/d = 2.02$ in the wake. As shown, the flow statistics for the uncontrolled flow obtained from the present LES are in good agreement with those from DNS by Lehmkühl et al. [44]. In particular, it is evident that the fluctuations of transverse velocities are significantly reduced in the near wake of the cylinder by the optimal tabs. This reduction of velocity fluctuations clearly indicates the suppression of the Kármán vortex shedding in the wake by tabs. In addition, the negative streamwise velocity by tabs observed at $x/d = 2.02$ is consistent with the increased recirculation length in Figure 12b.

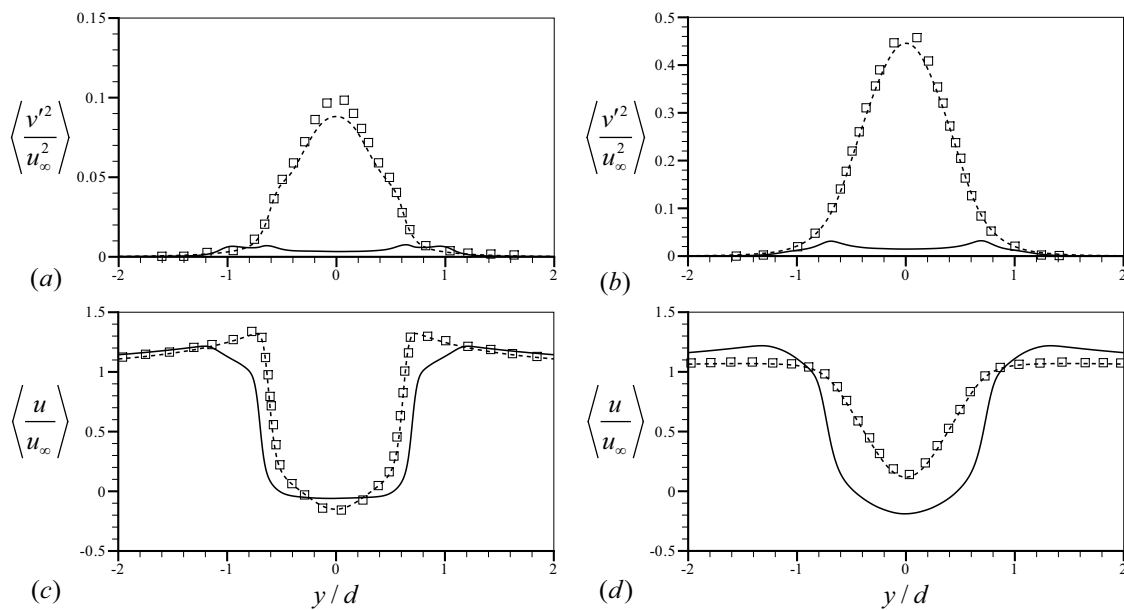


Figure 13. Mean square of transverse velocity fluctuations and mean streamwise velocity in the wake: (a,c) $x/d = 1.06$; (b,d) $x/d = 2.02$. Dashed line, cylinder without a tab; solid line, cylinder with tabs of $l_y/d = 0.2$ and $l_z/d = 0.3$; \square , direct numerical simulation [44]. Here, $\langle \rangle$ and $\langle \rangle'$ denote the mean and fluctuating quantities, respectively. The averaging for $\langle \rangle$ is taken over the spanwise direction and time.

3.3. Tabs in a Staggered Configuration

In the preceding sections, we focused on examining tabs attached to a circular cylinder in a non-staggered configuration where a pair of tabs are attached to the upper and lower surfaces of a circular cylinder at the same spanwise location as shown in Figure 2. In this section, we consider tabs in a staggered configuration as shown in Figure 14.

Figure 15 shows the time histories of drag and lift coefficients for flow over a circular cylinder with tabs in a staggered configuration, together with those for the uncontrolled flow. Here, the geometric parameters for tabs are the optimal ones ($l_y/d = 0.2$, $l_z/d = 0.3$, and $\lambda_z/d = 4$) obtained in a non-staggered configuration as discussed in Section 3.1. As shown in the figure, tabs in a staggered configuration reduce the mean drag and lift fluctuations ($C_D = 1.010$ and $C_{L_{rms}} = 0.052$) compared to those of the uncontrolled flow. However, these control performances are not as good as those for tabs in a non-staggered configuration (see Figure 4). Similar results were also observed in other 3D forcing methods [7,29].

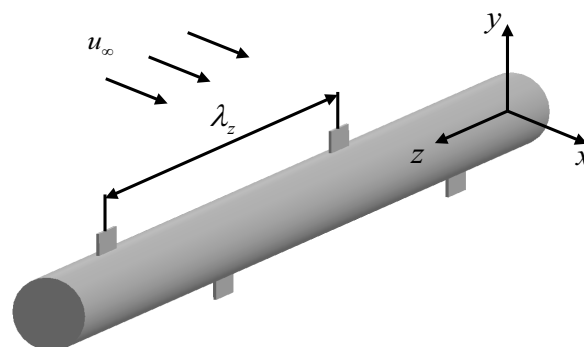


Figure 14. Schematic diagram of a circular cylinder with tabs in a staggered configuration.

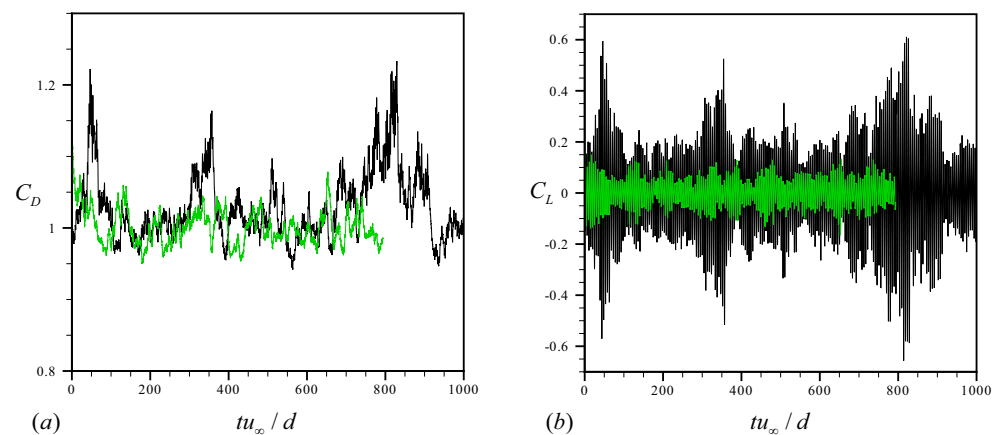


Figure 15. Time histories of drag and lift coefficients with and without tabs: (a) drag coefficient; (b) lift coefficient. Black line, cylinder without a tab; green line, cylinder with tabs of $l_y/d = 0.2$ and $l_z/d = 0.3$, and $\lambda_z/d = 4$ in a staggered configuration.

4. Conclusions

In this study, we investigated tabs applied to turbulent flow over a circular cylinder for the reductions of the mean drag and lift fluctuations. Tabs are small and thin passive devices consisting of a pair of tabs attached to the upper and lower surfaces of a circular cylinder near the flow separation. The Reynolds number considered was $Re = 3900$, based on the free-stream velocity and cylinder diameter. Large eddy simulations were performed using a dynamic global subgrid-scale eddy-viscosity model. A parametric study was carried out to find the optimal tab configuration for minimizing the mean drag and lift fluctuations. Parameters considered were the height and width of the tabs, and spanwise spacing between them. With the optimal parameters, the spanwise coherence of the vortex shedding behind the cylinder was effectively disrupted, resulting in three-dimensional vortical structures varying in the spanwise direction. As a result, the strength of the vortex shedding in the wake was successfully weakened, and the mean drag and lift fluctuations were significantly reduced by 14% and 95%, respectively.

Previous studies have shown that tabs are an effective passive device for reducing turbulent drag on two-dimensional bluff bodies with a blunt trailing edge having a fixed separation point [1,29]. Our investigation has also demonstrated that tabs are an effective tool for reducing drag on a circular cylinder in turbulent flow, even where the separation point is not fixed. These results suggest that tabs can be used for bluff bodies with nominally turbulent two-dimensional vortical structures, regardless of the characteristics of the separation location.

Other passive devices that provide 3D forcing, such as the wavy cylinder [22,23] and helically twisted elliptic cylinder [25,26], require significant modifications to the geometry of a circular cylinder, making their implementation challenging. In contrast, tabs can be easily attached to a bluff body without altering its original geometry, making them a more practical solution for controlling flow over a bluff body.

Author Contributions: Conceptualization, methodology, investigation: J.S., J.Y. and J.L.; validation, formal analysis, writing—original draft preparation, visualization: J.S., J.Y. and J.L.; writing—review and editing, supervision, project administration, funding acquisition: J.L. All authors have read and agreed to the published version of the manuscript.

Funding: This research was supported by the Basic Science Research Program through the National Research Foundation of Korea (NRF) funded by the Ministry of Education (2021R1F1A106326612). In addition, this work was supported by the Korea Ministry of Environment (MOE) as “Chemical Accident Advancement Project” (No. 2022003620005/1485018894). Computational resources were supported by the National Supercomputing Center with supercomputing resources (KSC-2021-CRE-0361).

Data Availability Statement: The data presented in this study are available from the corresponding author upon reasonable request.

Conflicts of Interest: The authors declare no conflict of interest.

Nomenclature

| | |
|--------------------|---|
| x | Streamwise direction |
| y | Transverse direction |
| z | Spanwise direction |
| t | Time |
| d | Cylinder diameter |
| u | Streamwise velocity |
| v | Transverse velocity |
| w | Spanwise velocity |
| p | Pressure |
| u_∞ | Free-stream velocity |
| ν | Kinematic viscosity |
| Re | Reynolds number |
| q | Mass source/sink |
| f_i | Momentum forcing |
| $\overline{(\)}$ | Filtered quantity |
| $\widetilde{(\)}$ | Test-filtered quantity |
| τ_{ij} | Subgrid-scale stress tensor |
| ν_T | Eddy viscosity |
| S_{ij} | Strain rate tensor |
| C_v | Vreman model coefficient |
| α_{ij} | Velocity gradient $\alpha_{ij} = \partial u_j / \partial x_i$ |
| u_i^* | Intermediate velocity |
| Δt | Time step |
| L_x | Streamwise domain size |
| L_y | Transverse domain size |
| L_z | Spanwise domain size |
| N_x | Number of streamwise grid points |
| N_y | Number of transverse grid points |
| N_z | Number of spanwise grid points |
| θ_t | Installation angle of tabs measured from the stagnation point |
| θ_s | Separation angle measured from the stagnation point |
| l_x | Tab thickness |
| l_y | Tab height |
| l_z | Tab width |
| λ_z | Spanwise distance between adjacent tabs |
| C_D | Drag coefficient |
| C_L | Lift coefficient |
| $C_{L_{rms}}$ | Coefficient of lift fluctuations |
| St | Strouhal number |
| L_r | Recirculation length |
| C_{p_b} | Base pressure |

References

1. Choi, H.; Jeon, W.P.; Kim, J. Control of Flow Over a Bluff Body. *Annu. Rev. Fluid Mech.* **2008**, *40*, 113–139. [[CrossRef](#)]
2. Bearman, P. Investigation of the flow behind a two-dimensional model with a blunt trailing edge and fitted with splitter plates. *J. Fluid Mech.* **1965**, *21*, 241–255. [[CrossRef](#)]
3. Bearman, P. The effect of base bleed on the flow behind a two-dimensional model with a blunt trailing edge. *Aeronaut. Q.* **1967**, *18*, 207–224. [[CrossRef](#)]
4. Nishioka, M.; Sato, H. Measurements of velocity distributions in the wake of a circular cylinder at low Reynolds numbers. *J. Fluid Mech.* **1974**, *65*, 97–112. [[CrossRef](#)]
5. Wood, C.J. The effect of base bleed on a periodic wake. *Aeronaut. J.* **1964**, *68*, 477–482. [[CrossRef](#)]

6. Min, C.; Choi, H. Suboptimal feedback control of vortex shedding at low Reynolds numbers. *J. Fluid Mech.* **1999**, *401*, 123–156. [[CrossRef](#)]
7. Kim, J.; Choi, H. Distributed forcing of flow over a circular cylinder. *Phys. Fluids* **2005**, *17*, 033103. [[CrossRef](#)]
8. Son, D.; Jeon, S.; Choi, H. A proportional–integral–differential control of flow over a circular cylinder. *Philos. Trans. R. Soc. A Math. Phys. Eng. Sci.* **2011**, *369*, 1540–1555. [[CrossRef](#)]
9. Wu, Z.; Choi, H. Modification of flow behind a circular cylinder by steady and time-periodic blowing. *Phys. Fluids* **2021**, *33*, 115126. [[CrossRef](#)]
10. Yun, J.; Lee, J. Active proportional feedback control of turbulent flow over a circular cylinder with averaged velocity sensor. *Phys. Fluids* **2022**, *34*, 095133. [[CrossRef](#)]
11. Stansby, P. The effects of end plates on the base pressure coefficient of a circular cylinder. *Aeronaut. J.* **1974**, *78*, 36–37.
12. Kwon, K.; Choi, H. Control of laminar vortex shedding behind a circular cylinder using splitter plates. *Phys. Fluids* **1996**, *8*, 479–486. [[CrossRef](#)]
13. Hwang, J.Y.; Yang, K.S.; Sun, S.H. Reduction of flow-induced forces on a circular cylinder using a detached splitter plate. *Phys. Fluids* **2003**, *15*, 2433–2436. [[CrossRef](#)]
14. Ain, Q.U.; Mahmood, R.; Awrejcewicz, J.; Siddique, I.; Majeed, A.H.; Pawłowski, W. Effectiveness of splitter plate to control fluid forces on a circular obstacle in a transient flow: FEM computations. *Sci. Rep.* **2022**, *12*, 13602. [[CrossRef](#)] [[PubMed](#)]
15. Shukla, S.; Govardhan, R.; Arakeri, J. Dynamics of a flexible splitter plate in the wake of a circular cylinder. *J. Fluids Struct.* **2013**, *41*, 127–134. [[CrossRef](#)]
16. Strykowski, P.J.; Sreenivasan, K.R. On the formation and suppression of vortex ‘shedding’ at low Reynolds numbers. *J. Fluid Mech.* **1990**, *218*, 71–107. [[CrossRef](#)]
17. Dalton, C.; Xu, Y.; Owen, J. The suppression of lift on a circular cylinder due to vortex shedding at moderate Reynolds numbers. *J. Fluids Struct.* **2001**, *15*, 617–628. [[CrossRef](#)]
18. Lee, S.J.; Lee, S.I.; Park, C.W. Reducing the drag on a circular cylinder by upstream installation of a small control rod. *Fluid Dyn. Res.* **2004**, *34*, 233. [[CrossRef](#)]
19. Tanner, M. A method for reducing the base drag of wings with blunt trailing edge. *Aeronaut. Q.* **1972**, *23*, 15–23. [[CrossRef](#)]
20. Rodriguez, O. Base drag reduction by control of the three-dimensional unsteady vortical structures. *Exp. Fluids* **1991**, *11*, 218–226. [[CrossRef](#)]
21. Petrusma, M.; Gai, S. The effect of geometry on the base pressure recovery of segmented blunt trailing edges. *Aeronaut. J.* **1994**, *98*, 267–274.
22. Ahmed, A.; Bays-Muchmore, B. Transverse flow over a wavy cylinder. *Phys. Fluids A Fluid Dyn.* **1992**, *4*, 1959–1967. [[CrossRef](#)]
23. Lam, K.; Wang, F.; Thus, R. Three-dimensional nature of vortices in the near wake of a wavy cylinder. *J. Fluids Struct.* **2004**, *19*, 815–833. [[CrossRef](#)]
24. Lim, H.C.; Lee, S.J. Flow control of a circular cylinder with O-rings. *Fluid Dyn. Res.* **2004**, *35*, 107. [[CrossRef](#)]
25. Jung, J.H.; Yoon, H.S. Large eddy simulation of flow over a twisted cylinder at a subcritical Reynolds number. *J. Fluid Mech.* **2014**, *759*, 579–611. [[CrossRef](#)]
26. Kim, W.; Lee, J.; Choi, H. Flow around a helically twisted elliptic cylinder. *Phys. Fluids* **2016**, *28*, 053602. [[CrossRef](#)]
27. Foss, J.K.; Zaman, K. Large-and small-scale vortical motions in a shear layer perturbed by tabs. *J. Fluid Mech.* **1999**, *382*, 307–329. [[CrossRef](#)]
28. Yoon, J.; Kim, J.; Choi, H. Control of laminar vortex shedding behind a circular cylinder using tabs. *J. Mech. Sci. Technol.* **2014**, *28*, 1721–1725. [[CrossRef](#)]
29. Park, H.; Lee, D.; Jeon, W.P.; Hahn, S.; Kim, J.; Kim, J.; Choi, J.; Choi, H. Drag reduction in flow over a two-dimensional bluff body with a blunt trailing edge using a new passive device. *J. Fluid Mech.* **2006**, *563*, 389–414. [[CrossRef](#)]
30. Park, H.; Jeon, W.P.; Choi, H.; Yoo, J.Y. Mixing enhancement behind a backward-facing step using tabs. *Phys. Fluids* **2007**, *19*, 105103. [[CrossRef](#)]
31. Kim, J.; Kim, D.; Choi, H. An immersed-boundary finite-volume method for simulations of flow in complex geometries. *J. Comput. Phys.* **2001**, *171*, 132–150. [[CrossRef](#)]
32. Park, N.; Lee, S.; Lee, J.; Choi, H. A dynamic subgrid-scale eddy viscosity model with a global model coefficient. *Phys. Fluids* **2006**, *18*, 125109. [[CrossRef](#)]
33. Lee, J.; Choi, H.; Park, N. Dynamic global model for large eddy simulation of transient flow. *Phys. Fluids* **2010**, *22*, 075106. [[CrossRef](#)]
34. Vreman, A. An eddy-viscosity subgrid-scale model for turbulent shear flow: Algebraic theory and applications. *Phys. Fluids* **2004**, *16*, 3670–3681. [[CrossRef](#)]
35. Germano, M.; Piomelli, U.; Moin, P.; Cabot, W.H. A dynamic subgrid-scale eddy viscosity model. *Phys. Fluids A Fluid Dyn.* **1991**, *3*, 1760–1765. [[CrossRef](#)]
36. Piomelli, U. High Reynolds number calculations using the dynamic subgrid-scale stress model. *Phys. Fluids A Fluid Dyn.* **1993**, *5*, 1484–1490. [[CrossRef](#)]
37. Kim, J.; Moin, P. Application of a fractional-step method to incompressible Navier–Stokes equations. *J. Comput. Phys.* **1985**, *59*, 308–323. [[CrossRef](#)]

38. Akselvoll, K. *Large Eddy Simulation of Turbulent Confined Coannular Jets and Turbulent Flow over a Backward-Facing Step*; Stanford University: Stanford, CA, USA, 1995.
39. Kim, K.; Baek, S.J.; Sung, H.J. An implicit velocity decoupling procedure for the incompressible Navier–Stokes equations. *Int. J. Numer. Methods Fluids* **2002**, *38*, 125–138. [[CrossRef](#)]
40. Beam, R.M.; Warming, R. An implicit factored scheme for the compressible Navier–Stokes equations. *AIAA J.* **1978**, *16*, 393–402. [[CrossRef](#)]
41. Yun, G.; Kim, D.; Choi, H. Vortical structures behind a sphere at subcritical Reynolds numbers. *Phys. Fluids* **2006**, *18*, 015102. [[CrossRef](#)]
42. Song, D.; Kim, W.; Kwon, O.K.; Choi, H. Vertical and torsional vibrations before the collapse of the Tacoma Narrows Bridge in 1940. *J. Fluid Mech.* **2022**, *949*, A11. [[CrossRef](#)]
43. Kravchenko, A.G.; Moin, P. Numerical studies of flow over a circular cylinder at $Re_D = 3900$. *Phys. Fluids* **2000**, *12*, 403–417. [[CrossRef](#)]
44. Lehmkuhl, O.; Rodríguez, I.; Borrell, R.; Oliva, A. Low-frequency unsteadiness in the vortex formation region of a circular cylinder. *Phys. Fluids* **2013**, *25*, 085109. [[CrossRef](#)]
45. Smirnov, N.; Betelin, V.; Shagaliev, R.; Nikitin, V.; Belyakov, I.; Deryuguin, Y.N.; Aksenov, S.; Korchazhkin, D. Hydrogen fuel rocket engines simulation using LOGOS code. *Int. J. Hydrogen Energy* **2014**, *39*, 10748–10756. [[CrossRef](#)]
46. Smirnov, N.; Betelin, V.; Nikitin, V.; Stamov, L.; Altoukhov, D. Accumulation of errors in numerical simulations of chemically reacting gas dynamics. *Acta Astronaut.* **2015**, *117*, 338–355. [[CrossRef](#)]
47. Choi, H.; Moin, P. Effects of the computational time step on numerical solutions of turbulent flow. *J. Comput. Phys.* **1994**, *113*, 1–4. [[CrossRef](#)]
48. Lam, K.; Lin, Y.; Zou, L.; Liu, Y. Investigation of turbulent flow past a yawed wavy cylinder. *J. Fluids Struct.* **2010**, *26*, 1078–1097. [[CrossRef](#)]
49. Franke, J.; Frank, W. Large eddy simulation of the flow past a circular cylinder at $Re_D = 3900$. *J. Wind. Eng. Ind. Aerodyn.* **2002**, *90*, 1191–1206. [[CrossRef](#)]
50. Jeong, J.; Hussain, F. On the identification of a vortex. *J. Fluid Mech.* **1995**, *285*, 69–94. [[CrossRef](#)]
51. Haller, G.; Beron-Vera, F.J. Coherent Lagrangian vortices: The black holes of turbulence. *J. Fluid Mech.* **2013**, *731*, R4. [[CrossRef](#)]
52. Haller, G. Lagrangian coherent structures. *Annu. Rev. Fluid Mech.* **2015**, *47*, 137–162. [[CrossRef](#)]
53. Haller, G.; Hadjighasem, A.; Farazmand, M.; Huhn, F. Defining coherent vortices objectively from the vorticity. *J. Fluid Mech.* **2016**, *795*, 136–173. [[CrossRef](#)]
54. Enrile, F.; Besio, G.; Stocchino, A. Shear and shearless Lagrangian structures in compound channels. *Adv. Water Resour.* **2018**, *113*, 141–154.
55. Fornberg, B. Steady viscous flow past a circular cylinder up to Reynolds number 600. *J. Comput. Phys.* **1985**, *61*, 297–320. [[CrossRef](#)]

Disclaimer/Publisher’s Note: The statements, opinions and data contained in all publications are solely those of the individual author(s) and contributor(s) and not of MDPI and/or the editor(s). MDPI and/or the editor(s) disclaim responsibility for any injury to people or property resulting from any ideas, methods, instructions or products referred to in the content.